

# UC Berkeley

## UC Berkeley Previously Published Works

### Title

Mitochondrial haplotype and mito-nuclear matching drive somatic mutation and selection throughout ageing.

### Permalink

<https://escholarship.org/uc/item/01h9z6cb>

### Journal

Nature Ecology and Evolution, 8(5)

### Authors

Serrano, Isabel

Hirose, Misa

Valentine, Charles

et al.

### Publication Date

2024-05-01

### DOI

10.1038/s41559-024-02338-3

Peer reviewed

# Mitochondrial haplotype and mito-nuclear matching drive somatic mutation and selection throughout ageing

Received: 8 March 2023

Accepted: 22 January 2024

Published online: 15 February 2024

 Check for updates

Isabel M. Serrano<sup>1</sup>, Misa Hirose<sup>2</sup>, Charles C. Valentine<sup>3</sup>, Sharon Roesner<sup>3</sup>, Elizabeth Schmidt<sup>3</sup>, Gabriel Pratt<sup>3</sup>, Lindsey Williams<sup>3</sup>, Jesse Salk<sup>3</sup>, Saleh Ibrahim<sup>4</sup> & Peter H. Sudmant<sup>1,5</sup>✉

Mitochondrial genomes co-evolve with the nuclear genome over evolutionary timescales and are shaped by selection in the female germline. Here we investigate how mismatching between nuclear and mitochondrial ancestry impacts the somatic evolution of the mitochondrial genome in different tissues throughout ageing. We used ultrasensitive duplex sequencing to profile ~2.5 million mitochondrial genomes across five mitochondrial haplotypes and three tissues in young and aged mice, cataloguing ~1.2 million mitochondrial somatic and ultralow-frequency inherited mutations, of which 81,097 are unique. We identify haplotype-specific mutational patterns and several mutational hotspots, including at the light strand origin of replication, which consistently exhibits the highest mutation frequency. We show that rodents exhibit a distinct mitochondrial somatic mutational spectrum compared with primates with a surfeit of reactive oxygen species-associated G > T/C > A mutations, and that somatic mutations in protein-coding genes exhibit signatures of negative selection. Lastly, we identify an extensive enrichment in somatic reversion mutations that ‘re-align’ mito-nuclear ancestry within an organism’s lifespan. Together, our findings demonstrate that mitochondrial genomes are a dynamically evolving subcellular population shaped by somatic mutation and selection throughout organismal lifetimes.

The mitochondrial genome (mt-genome) encodes for 13 proteins that are vital for the electron transport chain. However, more than 1,000 nuclear-encoded genes are necessary for mitochondrial assembly and function<sup>1</sup>. The required coordination between nuclear- and mitochondrial-encoded proteins drives the co-evolution of these two genomes<sup>2–4</sup>. This concerted evolution has been observed in both laboratory crosses and natural hybrids across a variety of species, including fruit flies<sup>5,6</sup>, marine copepods<sup>7,8</sup>, wasps<sup>9–11</sup>, yeast<sup>12,13</sup>,

eastern yellow robins<sup>14</sup>, swordtail fish<sup>15</sup> and teleost fish<sup>16</sup>. Hybrids often exhibit reduced fitness attributed to attenuated mitochondrial DNA (mtDNA) copy number<sup>17</sup>, mtDNA gene expression<sup>17,18</sup> and oxidative phosphorylation function<sup>6–8,10</sup>. In natural hybrids, the genetic ancestry at nuclear-encoded mitochondrial genes is highly differentiated between populations that have distinct mitochondrial haplotypes (mt-haplotypes)<sup>14</sup>. In human admixed populations, mito-nuclear ancestral discordance has been shown to correlate with reductions in mtDNA

<sup>1</sup>Center for Computational Biology, University of California, Berkeley, CA, USA. <sup>2</sup>Lübeck Institute of Experimental Dermatology, University of Lübeck, Lübeck, Germany. <sup>3</sup>TwinStrand Biosciences, Seattle, WA, USA. <sup>4</sup>College of Medicine, Khalifa University, Abu Dhabi, UAE. <sup>5</sup>Department of Integrative Biology, University of California, Berkeley, CA, USA. ✉e-mail: [psudmant@berkeley.edu](mailto:psudmant@berkeley.edu)

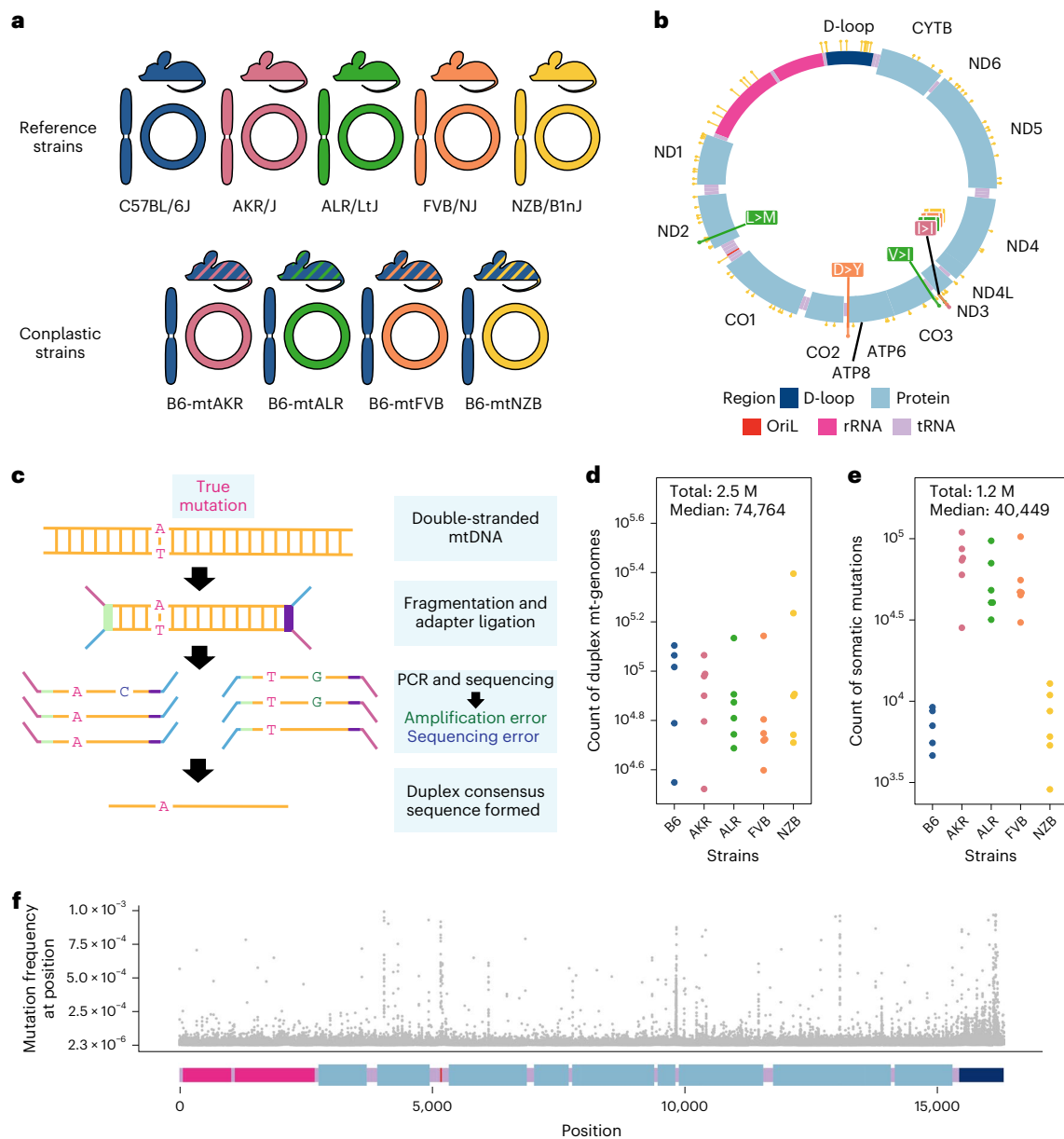


**Fig. 1 | Overview of experimental design. a**, Maternal donors were selected from common inbred strains (CISs) containing non-synonymous variants with functional effects. Females from these CISs (pink, green and orange) were backcrossed with a C57BL/6J mouse (blue). This process was repeated with a wild-inbred strain (yellow). The result of these crossings are conplastic mouse strains (denoted by the striped mice). These conplastic strains have identical B6 nuclear (linear) genetic backgrounds but differ by variants along their mt-genomes (circular). **b**, B6-mtAKR (pink), B6-mtALR (green) and B6-mtFVB (orange) differ from wild type by one to three non-synonymous variants. B6-mtNZB (yellow) contains 91 variants distributed across the mt-genome (14 non-synonymous and 56 synonymous mutations). The synonymous mutation in *MT-ND3* is shared across conplastic strains. For a more detailed account of these variants and their associated phenotypes reference (Supplementary Table 1). **c**, Ultrasensitive duplex sequencing (DupSeq) was used to profile mt-genomes from conplastic mice. DupSeq has an unprecedented error rate of  $<10^{-7}$ . Each double-stranded mtDNA fragment is distinctly tagged with a unique molecular barcode, allowing for the computational construction of a duplex consensus sequence. As a result,

both polymerase chain reaction (PCR) and sequencing errors are filtered from the data. **d**, The count of duplex mt-genomes sequenced was calculated for each experimental condition ( $n = 29$  conditions;  $n = 4$  mice for every condition with three mice for B6-Young-Heart). The duplex read depth at each position was aggregated across samples in a condition to quantify the duplex depth per condition. The average duplex read depth across the mt-genome was then calculated. An estimated 2.5 million mt-genomes were duplex sequenced with a median of 74,764 mt-genomes duplex sequenced per condition. **e**, Approximately 1.2 million variants were identified with a median of 40,449 variants per condition. The count of variants was aggregated across samples in a condition. Mutations present at conplastic haplotype sites were filtered from the analysis. **f**, The mutation frequency for each position is mapped along a linear representation of the mt-genome. Each point denotes the mutation frequency for an experimental condition at the given position in the mt-genome. Legends for the mt-genome map are consistent with those in **b**. Positions with a mutation frequency greater than  $1 \times 10^{-3}$  were excluded from this analysis.

copy number<sup>19</sup>. Additionally, de novo germline mitochondrial mutations in admixed human populations exhibit a bias towards concordance with nuclear ancestry<sup>20</sup>. In somatic tissues, the nuclear genome has been shown to influence the segregation of mtDNA haplotypes

in a tissue-specific manner<sup>21–23</sup>. Together, these studies highlight the functional importance of mito-nuclear ancestral concordance. However, the impact of these genomic interactions on somatic mutation and selection has not been studied.

As healthy cells age, they accumulate nuclear and mtDNA damage as a result of environmental exposures and cellular processes<sup>24</sup>. mtDNA has a 10- to 100-fold higher de novo germline mutation rate than nuclear DNA<sup>20,25,26</sup> due to its lack of protective histones, a higher replication rate and less effective DNA damage repair mechanisms<sup>27</sup>. Individual cells can contain hundreds to thousands of mt-genomes<sup>28,29</sup>, presenting a dynamic subcellular population that is highly susceptible to mutation. While the relationship between mutations in the mt-genome and ageing remains unclear<sup>30,31</sup>, increased mtDNA damage has been associated with many ageing phenotypes and several age-related diseases<sup>30,32</sup>. Yet, profiling low-frequency mutations in this population of mt-genomes has historically been challenging with most technologies limited to variants segregating at a frequency >1% (refs. 26,33). More recently, several studies have employed duplex sequencing<sup>33</sup> to capture mutations with an error rate of  $<1 \times 10^{-7}$ . These works have examined several different species and confirmed a robust age-associated increase in mtDNA somatic mutation frequency<sup>34–37</sup>; identified that mitochondrial somatic mutations stem from the replication process either via DNA polymerase gamma misincorporations or spontaneous DNA deamination of cytosine and adenine<sup>34–37</sup>; and observed tissue-specific somatic mutation rates<sup>36,37</sup>.

In this Article, we investigate the impact of mitochondrial ancestry (mt-ancestry) and tissue type on the somatic evolution of the mt-genome through age. To explore how mt-haplotype and mito-nuclear genomic interactions shape the mt-genome mutational landscape, we utilize a panel of mouse strains that have identical nuclear genomes but differ in their mt-haplotypes (conplastic strains). We sample the brain, heart and liver of these conplastic strains and the wild type (C57BL/6J) in young and aged individuals. These tissues are physiologically distinct yet some of the most metabolically active, allowing us to study how evolutionary processes unfold in different molecular contexts. We use duplex sequencing to profile mt-genomes at an unprecedented level of depth and accuracy, allowing us to identify mutational hotspots and characterize the mutational spectrum. We use these results to discern signatures of selection acting to shape the mt-genome through age and confirm the existence of somatic mutations that work to re-align mito-nuclear ancestry at short, within-lifespan, evolutionary timescales. Together, these findings characterize somatic evolution in the context of an organelle implicated in ageing and age-related phenotypes.

## Results

### Duplex sequencing of 2.5 million mt-genomes

To investigate how mt-haplotype and mito-nuclear concordance influence the distribution of mt-genome somatic mutations, we employed a panel of conplastic mouse strains. These strains are inter-population hybrids developed by crossing common laboratory strains with the C57BL/6J (B6) mouse line<sup>38</sup>. Each conplastic mouse strain carries a unique mt-haplotype on a C57BL/6J nuclear genomic background (Fig. 1a). This fixed nuclear background enables us to attribute differences in somatic mutation to changes in mt-haplotype. Alongside a wild-type B6 mouse, we used four conplastic mouse strains that exhibit changes in metabolic content and processes, or altered ageing phenotypes (Supplementary Table 1). Three of these conplastic mouse strains differ from the C57BL/6J mt-haplotype by just 1–3 non-synonymous variants, while a single strain (NZB) contains 91 variants distributed across the mt-genome (Fig. 1b and Supplementary Table 1). We sampled brain, liver and heart tissues from each of these mouse strains in young (2–4 months old) and aged (15–22 months old) individuals to examine how ageing and metabolic demands shape the mutational spectrum in distinct physiological contexts. In total, three tissues were sampled from five mouse strains at two different ages over three to four replicates per condition, resulting in  $n = 115$  samples.

To capture low-frequency variants and accurately portray the somatic mutational landscape, we used ultrasensitive duplex sequencing to profile mt-genomes across different experimental conditions<sup>33</sup>.

This approach works by tagging double-stranded mtDNA sequences with molecular identifiers and computationally constructing a duplex consensus sequence (Fig. 1c) resulting in error rates of  $\sim 2 \times 10^{-8}$ . Importantly, duplex sequencing data can contain an artificial enrichment of G > T, C > T and G > C mutations resulting from DNA damage during sequencing preparation steps<sup>39</sup>. To exclude potential erroneous calls, we trimmed 10 bp from our duplex reads (Supplementary Note 1 and Supplementary Fig. 1). Additionally, we analysed the mutational spectra for atypical imbalances of complementary mutation types and compared our mutation type proportions with a previously published study<sup>37</sup> (Supplementary Figs. 2 and 3, and Supplementary Tables 2 and 3). Using this approach, we profiled 2.5 million duplex mt-genomes, with a median of 74,764 duplex mt-genomes sequenced per condition (strain  $\times$  tissue  $\times$  age) (Fig. 1d). This resource allows for the detection of somatic mutations at a frequency of  $4 \times 10^{-6}$ .

Duplex reads from each sample were mapped to the mouse mt-genome (mm10) and variants were called using a duplex sequencing processing pipeline (Methods). Mutations overlapping conplastic haplotype sites were filtered out. In total we identified 1,171,918 somatic variants, with a median of 40,449 somatic mutations per condition (Fig. 1e). From these 1.2 M mutations, 81,097 mutations are unique events. These variants were distributed across the entirety of the mt-genome (Fig. 1f).

### Haplotype- and tissue-specific mutational hotspots

Somatic mutations accumulate with age across both nuclear and mitochondrial genomes<sup>24</sup>. We observed this trend consistently across tissues and mt-haplotypes with the mutation frequency on average 2-fold higher in aged mice compared with young mice (Fig. 2a). This trend was most pronounced in the liver (2.5-fold higher) and smallest in the heart (1.6-fold higher). Additionally, the heart sustained the lowest mutation frequency on average (Fig. 2a), despite its high metabolic demands as demonstrated by its higher mitochondrial copy number (Supplementary Fig. 4). Comparing age-associated mutation rates across different strains we find AKR, ALR and NZB all exhibit strain-specific mutation rates (Supplementary Table 4;  $P$  value  $< 0.01$ , log-link regression). The FVB strain, which only differs from B6 at two sites (Fig. 1b) showed no evidence of strain-specific mutation rates compared with wild type. AKR and ALR strains had lower mutation rates across all tissues, while NZB exhibited strong increases in the brain and decreases in the heart.

We next examined the variation in mutation rates and frequencies across different regions of the mt-genome (Fig. 2b,c). The density of mutations was lowest in functional coding regions (protein-coding, ribosomal RNA (rRNA) and transfer RNA (tRNA) segments) while the *D-loop* exhibited a significantly higher mutation frequency in both young (6.4-fold,  $P = 3.4 \times 10^{-9}$ ; two-tailed  $t$ -test) and aged (4.5-fold,  $P = 8.6 \times 10^{-8}$ ; two-tailed  $t$ -test) mice. However, we further found that the light strand origin of replication (*OriL*) had an even higher average mutation frequency, 40- to 22-fold in excess of the functional coding regions in young and aged mice, respectively (Fig. 2b). This *OriL* hotspot of mutation was most pronounced in aged wild-type B6 mice. The *OriL* was recently noted as a mutational hotspot in macaque liver, but not in oocytes or muscle in that species<sup>36</sup>. In contrast, we find the *OriL* to exhibit elevated mutation frequencies across the brain, heart and liver.

Our initial inspection of the overall distribution of mutations across the mt-genome highlighted several distinct clusters appearing at finer-scale resolution than our simple functional classification groups (Fig. 1f). To resolve these putative mutational hotspots we quantified the average mutation frequency in 150-bp sliding windows over the mt-genome independently across tissues and mt-haplotypes (Fig. 3a). In addition to the *D-loop*, this analysis identified mutational hotspots in *OriL*, *MT-ND2* and *MT-tRNA<sup>Arg</sup>*.

The *OriL* forms a stem-loop structure that is conserved across species<sup>40</sup> but differs markedly in its sequence. We identified mutations throughout the loop and 5' end of the stem with the highest mutation

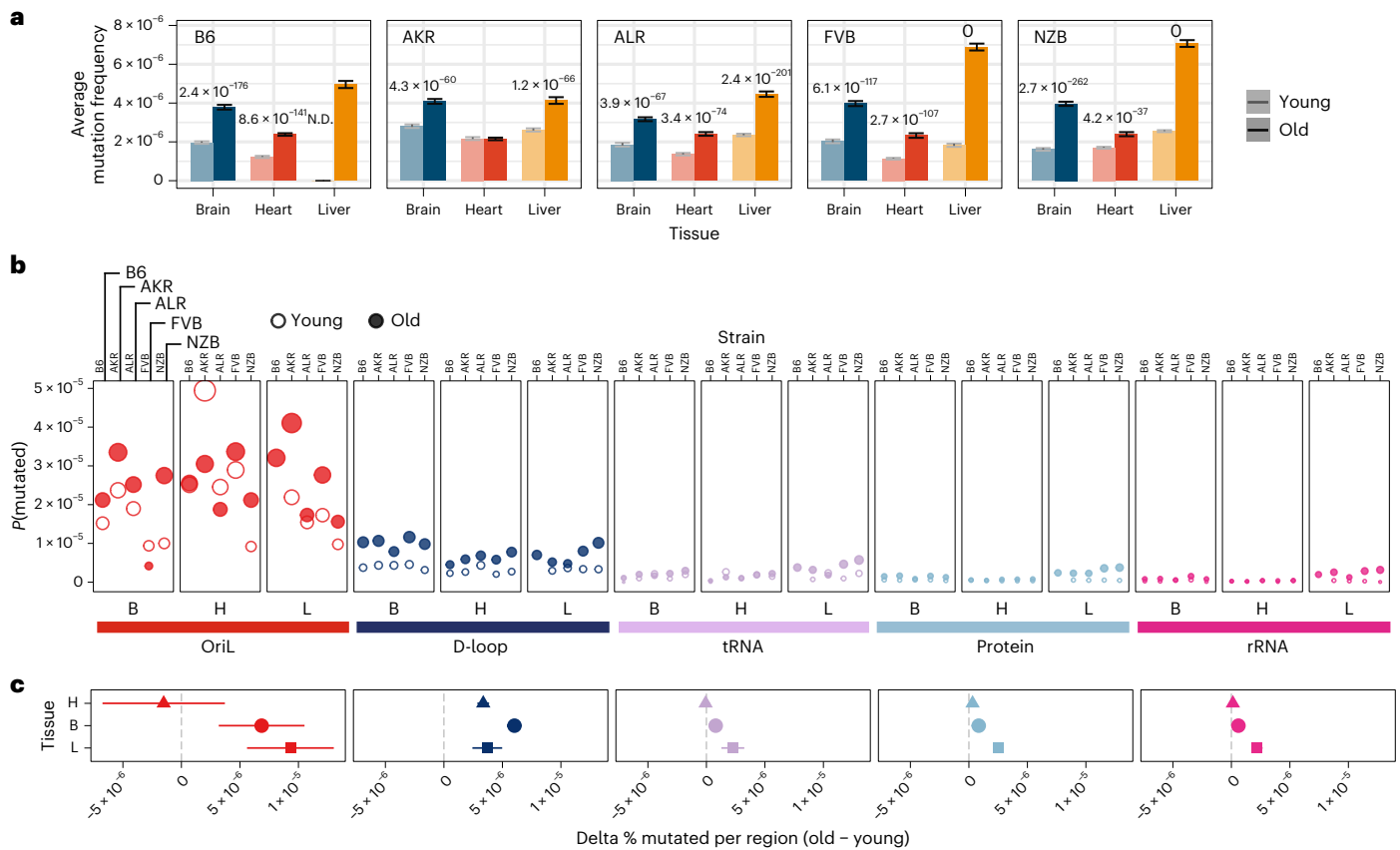


**Fig. 2 | Region-specific changes in somatic mutation frequency with age.**

**a**, The average mutation frequency for young (light) and aged (dark) mice in each experimental condition ( $n = 29$  conditions;  $n = 4$  mice for every condition with three mice for B6-Young-Heart). Mutation counts and duplex depth were aggregated across samples for each condition. The mutation frequency for each position along the mt-genome was calculated by dividing the total count of alternative alleles by the duplex read depth at the position. The bar denotes the average mutation frequency across positions in the mt-genome. Error bars denote the 95% Poisson confidence intervals.  $P$  values indicate experimental conditions with a significant age-associated increase in mutation frequency. The  $P$  values were calculated from a log-linear regression and adjusted using a Bonferroni multiple hypothesis correction. **b**, The mt-genome was categorized into regions: OriL (red), D-loop (dark blue), tRNAs (purple), protein coding (light

blue) and rRNAs (magenta). For each region, the probability of mutation was calculated as the total count of mutations normalized by the region length in bp multiplied by the average duplex read depth across the region. Fill indicates age group: young (hollow circles) and aged (filled circles). **c**, The difference in per cent bp mutated between young and aged mice for each mt-haplotype ( $n = 5$  delta values for brain and heart;  $n = 4$  delta values for liver). The shape denotes the average difference in per cent bp mutated with age across mt-haplotypes. Error bars showcase the standard error of the mean. Positions that exceeded a mutation frequency of  $1 \times 10^{-3}$  were excluded from these analyses. For **b** and **c**, frequencies were normalized for sequencing depth across conditions at each position, and mutation counts and duplex depth were aggregated across samples in an experimental condition to calculate the per cent bp mutated.

frequencies corresponding to changes in the size of the stem-loop (Fig. 3b). Repeated mutations of the 5' end of the stem-loop structure mirror those observed in macaque liver in a recent study<sup>36</sup>, though the sequence of the stem differs between these two species. Thus, the conserved structure of the *OriL* appears to drive convergent mutational phenotypes between species.

The *MT-ND2* mutation hotspot consists of a frameshift-inducing A insertion (INS) or deletion (DEL) that introduces a premature stop codon (Fig. 3c). This stop codon reduces the length of the final protein product by more than 250 amino acids, probably severely impacting its function. This mutation increases in frequency with age across all strains except NZB. The final mutation hotspot we identified is localized to an eight-nucleotide stretch of *MT-tRNA<sup>Arg</sup>* (Fig. 3d). These nucleotides correspond to the 5' D-arm stem-loop of the tRNA and constitute primarily A INS 2-4 nucleotides long. Computational tRNA structure predictions show that these mutations increase the size of the loop (Supplementary Figs. 5 and 6)<sup>41</sup>. This mutational hotspot exhibits strong strain specificity with B6 exhibiting few somatic mutations in this A-repeat stretch. The D-arm plays a critical role in creating the tertiary structure of tRNAs<sup>42,43</sup> potentially contributing to its constraint in the wild type. Together, these results highlight the emergence of

distinct mutational hotspots in mt-genomes occurring in age- and strain-specific contexts, and implicating both DNA and RNA secondary structures.

### Replication errors and DEL distinguish aged mt-genomes

Somatic mutations are caused by various molecular processes that lead to DNA damage, each of which exhibits a distinct mutational signature<sup>44</sup>. To identify sources of mitochondrial somatic mutation, we categorized mutations into single nucleotide variants (SNVs), DEL and INS (Fig. 4a). SNVs were further classified into the six possible substitution classes (Fig. 4b). Overall, SNVs were the predominant somatic mutation type, with a fivefold higher average mutation frequency than DEL and INS in both young and aged individuals (Supplementary Fig. 7). The most abundant mutation type observed was  $G > A/C > T$ , which is indicative of replication error or cytosine deamination to uracil<sup>45,46</sup> (Fig. 4b). The reactive oxygen species (ROS) damage signature of  $G > T/C > A$  (ref. 47) was the second most predominant mutation type. All somatic mutation types were used to identify two dominant mutational signatures using a multinomial bayesian inference model<sup>48</sup> (Fig. 4c). These signatures explained the bulk of the variation across samples (Supplementary Fig. 8).

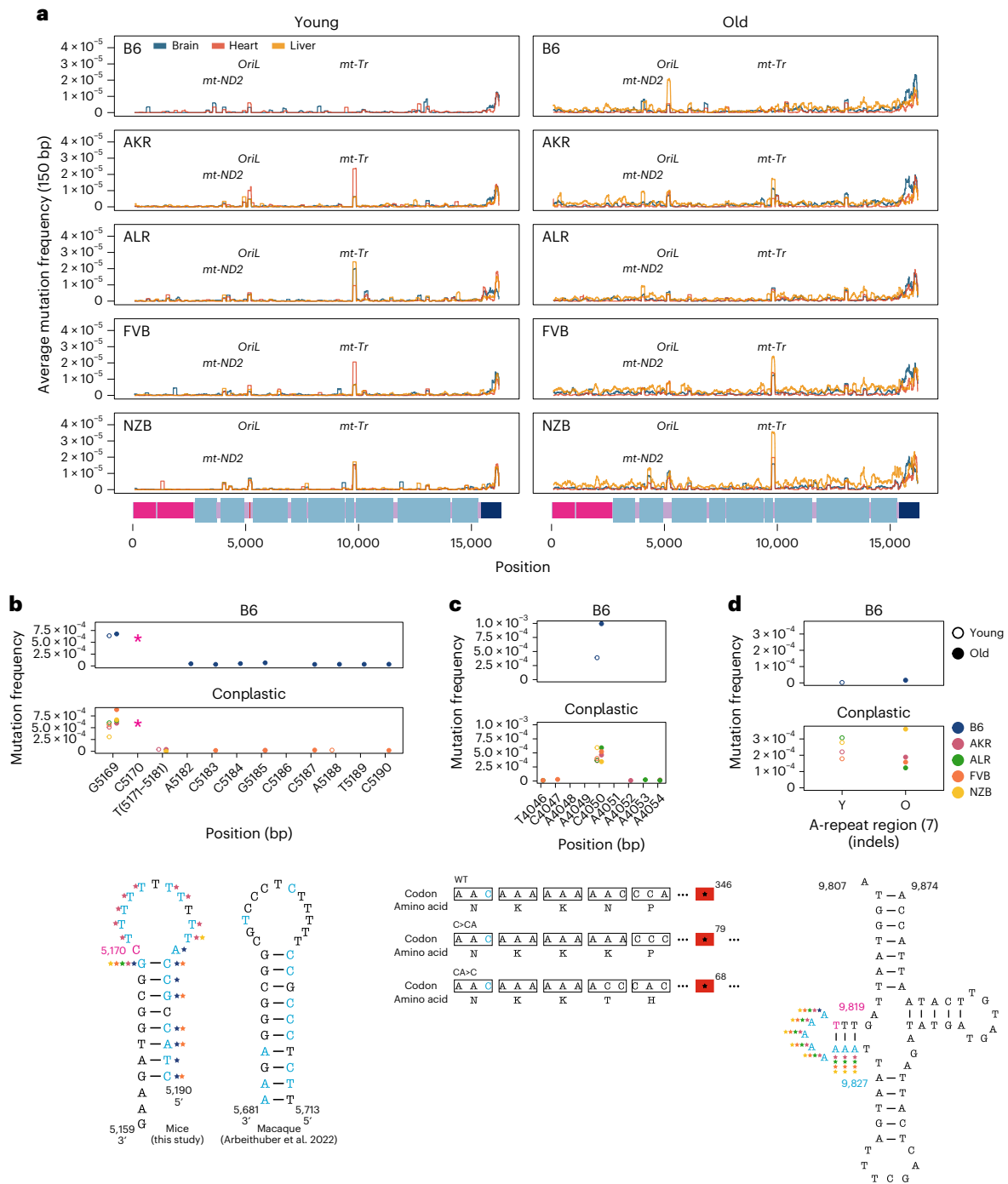


**Fig. 3 | Haplotype-specific peaks of mutation along the mt-genome. a**, The average mutation frequency was calculated in 150-bp sliding windows for each strain and tissue independently. Each line represents a tissue: brain (blue), heart (red) and liver (orange). Regions with shared mutation frequency peaks in at least three mouse strains are labelled. **b**, The high-frequency region in the light strand origin of replication (*OriL*) is highlighted. For positions 5,171–5,181 the mutation frequency for the T-repeat region is calculated as the sum of mutations across this region divided by the sum of the duplex depth across positions. Each colour denotes a different strain: B6 (blue), AKR (pink), ALR (green), FVB (orange) and NZB (yellow). The average frequency in young (left, hollow points) and aged (right, filled points) mice is compared. The schematic compares the *OriL* structure in mice with that of macaques<sup>36</sup>. Positions with a mutation frequency  $>1 \times 10^{-3}$  are in magenta, while other positions exhibiting mutations are denoted in light blue. In the macaque *OriL* diagram, variant hotspots are denoted in light blue. Stars represent strains that have mutations present at a

given position. **c**, The high-frequency region in *MT-ND2* is highlighted. Colour, shape and calculation of the average mutation frequency are similar to those in **b**. A schematic demonstrating the sequence and codon changes that result from the indels at position 4,050: premature stop codons at codon 79 and 68 for C > CA and CA > C, respectively. The superscript denotes the position of the premature stop codon in the amino acid sequence. **d**, The mutation frequency for *MT-tRNA<sup>Arg</sup>* from bp positions 9,820–9,827, which is an A-repeat region. The mutation frequency for the A-repeat region is calculated as the sum of mutations across this region divided by the sum of the duplex depth across positions. The diagram of *MT-tRNA<sup>Arg</sup>* highlights in magenta the location of a fixed variant in NZB, which is a high heteroplasmic variant in the other mouse strains. Positions that have mutations in this region are in light blue. Positions that exceeded a mutation frequency of  $1 \times 10^{-3}$  were excluded from these analyses. Frequencies were normalized for sequencing depth across conditions at each position.

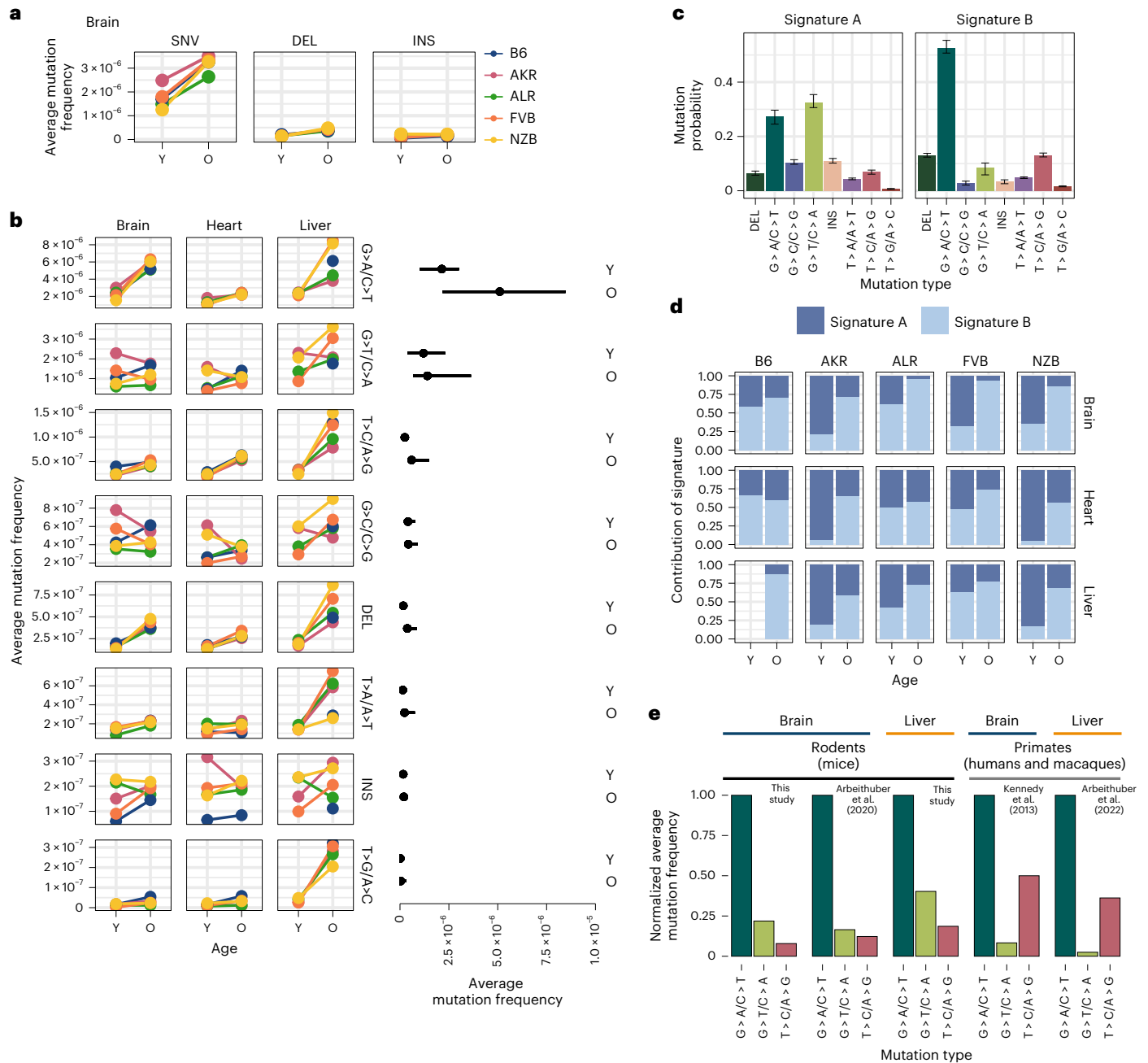


**Fig. 4 | Characterizing the mt-genome mutational landscape.** **a**, The average mutation frequency is compared between mt-haplotypes for different classes of mutations: SNVs, DEL and INS. The average mutation frequency was calculated as the total mutation count in a class divided by the total duplex bp depth. Each point denotes the average mutation frequency across the mt-genome for young (Y) and aged (O) mice in each strain (B6 (blue), AKR (pink), ALR (green), FVB (orange) and NZB (yellow)). The connecting line demonstrates the change in frequency from young to aged mice. Mutation counts and duplex depth were aggregated across samples for each condition to calculate the average mutation frequency. Results for the brain are featured, which showcase trends observed in the heart and liver, as well (Supplementary Fig. 7). **b**, SNVs were further classified into point mutation types. Each point denotes the average mutation frequency for the given mutation type across the mt-genome for each mouse strain (colour key as in **a**). The average frequency for point mutations was calculated as the total count of mutations of the given type divided by the duplex bp depth for the reference nucleotide. The average mutation frequency for DEL and INS was calculated as the total mutation count in these classes divided by the total duplex bp depth. Mutation types are ordered by descending average mutation frequencies. The range in frequency across experimental conditions (strain  $\times$  tissue,  $n = 15$  conditions for brain and heart;  $n = 14$  conditions for liver) for each

mutation type is shown. For each mutation type, the segment extends from the minimum to the maximum frequency across experimental conditions in the age group. Each point in the segment denotes the median frequency across conditions. **c**, Mutational signatures were extracted from mutation type counts for each experimental condition using sigfit. Two mutational signatures were identified. The probability that a mutation type contributed to a signature is showcased. Each bar denotes the estimated probability of a mutation type comprising the signature with error bars denoting the 95% confidence interval of each estimate. **d**, The presence of the mutational signatures was estimated for each condition (signature A dark blue, signature B light blue). The contribution of each mutational signature is compared across age. **e**, The frequency of the three most abundant mutation types were compared across mice, macaques and humans for the brain and liver. Mutation frequencies were normalized by the frequency of the  $G > A/C > T$  mutation in their respective study. All studies used duplex sequencing to profile mutations in the mt-genome. For the mutation frequencies in our study, we only show the mutation frequencies for B6. Refer to Supplementary Fig. 9a for frequencies across all strains, tissues and young mice. For all analyses, mutation counts and duplex bp depth were aggregated across samples in an experimental condition. Positions with mutation frequencies greater than  $1 \times 10^{-3}$  were omitted from these analyses.

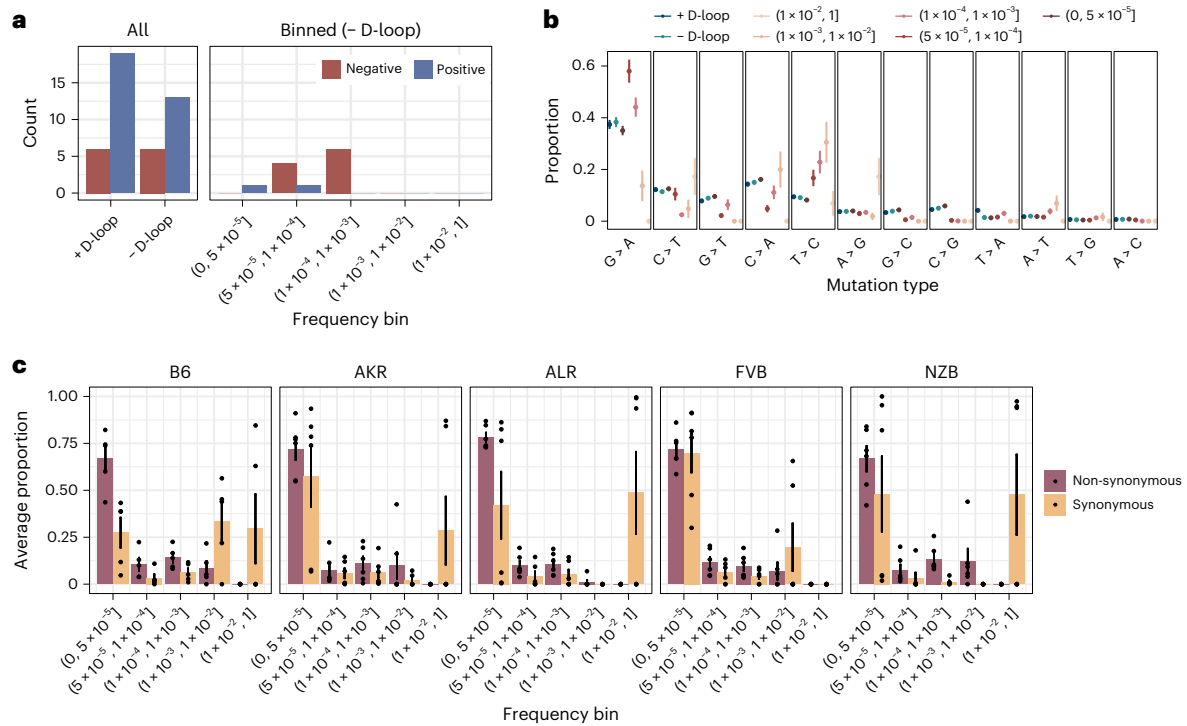


**Fig. 5 | Negative selection shapes the mt-genome. a**, The count of genes under positive (blue) and negative (red) selection. Mutations and mutation type proportions were quantified in three different ways: (1) all mutations, without consideration of mutation frequency or mt-genome position, (2) all mutations excluding the *D-loop*, and (3) mutation counts binned by mutation frequency, excluding the *D-loop*. Mutations with a frequency greater than  $1 \times 10^{-3}$  were excluded from analyses 1 and 2. **b**, The proportion of each mutation type. Proportions are calculated as the count of mutations of each type divided by the total count of mutations in a given bin. The average mutation type proportion across experimental conditions ( $n = 29$  conditions; strain  $\times$  tissue  $\times$  age) is shown with error bars denoting the standard error of the mean. In blue are proportions for the aggregated mutation counts with (dark blue) and without

(light blue) the *D-loop*. Mutations are ordered in descending order of average mutation frequency. **c**, The frequency spectra for non-synonymous (purple) and synonymous (orange) mutations. The bar denotes the average proportion of non-synonymous and synonymous mutations in a bin. The proportion is calculated as the count of non-synonymous or synonymous mutations in a frequency bin relative to the total count of non-synonymous or synonymous mutations across all bins. The average proportion is taken across tissues and age in a strain ( $n = 6$  except for B6, where  $n = 5$ ). Each point represents the proportions that compose the average. The error bars denote the standard error of the mean. For these analyses mutation counts were aggregated across samples in an experimental condition.

The accumulation of somatic mutations with age is a well-known phenomenon that has been hypothesized to play key roles in the aetiology of lifespan<sup>49</sup>. We observed that four out of the eight mutation types significantly increased in frequency with age (adjusted  $P$  value  $< 0.01$ ; Fisher's exact test with a Benjamini–Hochberg correction) (Fig. 4b and Supplementary Table 5) across all tissues, with  $T > A/A > T$  mutations additionally exhibiting age-associated accumulation in the liver but not in brain or heart. These age-associated signatures compose *mutational signature B* (Fig. 4c), which overall distinguishes aged from young samples (Fig. 4d). The consistency of these signatures across both mutations and mt-haplotypes suggest that these mutations occur in a ‘clock-like’ fashion in mitochondria over lifespan.

In contrast, INS,  $G > C/C > G$ , and  $G > T/C > A$  mutations did not exhibit consistent age-associated patterns. These mutations are represented in *mutational signature A* (Fig. 4c). Of particular note, the  $G > T/C > A$  and  $G > C/C > G$  mutation patterns are associated with ROS damage. An increase in ROS damage has been hypothesized to play an important role in ageing. Nonetheless, we do not find evidence of an increase in ROS-associated damage with age. Previous works in the human brain<sup>34,50</sup>, macaque tissues<sup>36</sup> and various mouse tissues<sup>35,37</sup> have also observed a lack of ROS-associated damage with age.

### Species-specific mitochondrial mutational signatures

While the overwhelming majority of research into somatic mutation rates and profiles has focused on humans, comparative analyses can provide insight into the evolutionary processes that have shaped

mutation. To determine if mitochondrial somatic mutation exhibited species-specific patterns, we compared several recent studies that duplex sequenced mt-genomes in multiple mouse, human and macaque tissues<sup>34–37</sup>. In our dataset, we found the relative magnitude of mutation frequencies to be consistent across tissues and mt-haplotypes with the  $G > A/C > T$  and  $G > T/C > A$  mutations being the most abundant (Fig. 4b and Supplementary Fig. 9a). This signature is consistent with other duplex sequencing-based analyses of mitochondrial mutations in young and aged mouse brain, muscle, kidney, liver, eye, heart and oocytes (Fig. 4e and Supplementary Fig. 9b,c)<sup>35,37</sup>. However, profiling of mitochondrial mutation signatures in several young and aged human brains noted transitions,  $G > A/C > T$  and  $T > C/A > G$ , to be the most abundant mutation signatures<sup>34</sup> (Fig. 4e). We find that this pattern is also recapitulated in a recent dataset of mitochondrial somatic mutation in macaque muscle, heart, liver and oocytes (Fig. 4e and Supplementary Fig. 9d)<sup>36</sup>. These differences in mutational signatures were observed between primate and rodent species from duplex sequencing data generated independently by two research groups, emphasizing the reproducibility of this phenomenon. Together, these results suggest that rodent and primate mt-genomes are subject to distinct mutational processes, potentially as a cause or effect of physiological differences between these lineages.

### Negative selection shapes mitochondrial mutation frequencies

While only 13 proteins are encoded on the mt-genome, these products are vital components of the electron transport chain. Given their



importance, we investigated whether selection was acting to shape the mutational landscape of the mt-genome.

We calculated the  $\frac{hN}{hS}$  statistic<sup>51</sup>, which is akin to the  $\frac{dN}{dS}$  statistic, for every gene across our 29 experimental conditions. For each condition, we also simulated the expected distribution of  $\frac{hN}{hS}$  ratios using the observed mutation counts and mutational spectra (Supplementary Fig. 10). Prima facie, the mt-genome appeared to be shaped predominantly by positive selection (Fig. 5a). However, differences in the mutation spectrum between mutational hotspots, including the *D-loop*, could bias the simulated null distribution of mutations. Indeed, mutation spectra were substantially different between *D-loop* and non-*D-loop* mutations, as well as among mutations at different frequencies (Fig. 5b). Furthermore, quantifying the allele frequency spectrum of non-synonymous and synonymous mutations revealed that non-synonymous substitutions were strongly enriched at low frequencies compared with synonymous substitutions indicating that negative selection is probably preventing these mutations from increasing in frequency (Fig. 5c).

We thus performed our  $\frac{hN}{hS}$  analyses independently in different frequency bins (Fig. 5a) revealing primarily signatures of negative selection. From the 12 possible cases of selection, 75% were in conplastic mice, and both cases of positive selection were in NZB mice. Genes with selective signatures include *MT-CO1* (3), *MT-CO3* (1), *MT-CYTB* (1), *MT-ND2* (1) and *MT-ND5* (6), whose protein products compose complexes I, III and IV of the electron transport chain. Intriguingly, signatures of negative selection in *MT-ND5* were observed across all five strains in our experiment. Taken together, these results indicate that negative selection dominates the distribution of mutations in mt-genomes, though this signature is predominantly found at intermediate frequencies.

### Mito-nuclear mismatches drive somatic reversion mutations

Mismatching of mitochondrial and nuclear haplotypes, such as in hybrid populations, has been associated with reductions in fitness<sup>5–13,15</sup>. The conplastic strains we employ are hybrids with mismatched nuclear and mt-genome ancestries. Since hybrids often demonstrate reduced fitness as a result of mito-nuclear discordance, we reasoned that at sites where the conplastic mt-genome differed from the B6 mt-genome (haplotype sites), there may be a preference for ‘reversion’ mutations to the B6 allele (Fig. 6a).

We hypothesized that if somatic selection were to favour the B6 allele, then reversions would occur at a higher rate than background mutations (Supplementary Table 6). Three of the strains have several fixed haplotype sites in their mt-genomes, ALR, FVB and NZB. We find that, in ALR and FVB strains, haplotype sites were among the most mutated sites in the mt-genome, with sixfold and sevenfold higher average mutation frequency than non-haplotype sites, respectively (Fig. 6b, adjusted *P* values < 0.001). In NZB, which differs from B6 at 91 locations, these haplotype sites had 122-fold higher mutation frequency than background (adjusted *P* values <  $1 \times 10^{-53}$ ). The overwhelming majority (75–100%) of these mutations are reversions to the B6 allele with the specific reversion mutation occurring significantly more than expected by chance (Supplementary Table 7). These results demonstrate the extreme selective pressures impressed by nuclear–mitochondrial matching to re-introduce the ancestral allele.

We next hypothesized that if somatic selection were to favour reversions, these B6 reversion alleles should increase in frequency with age. We quantified the relative change in reversion frequencies across strains and found that in ALR and FVB all unique fixed sites exhibited a significant increase in the reversion allele frequency with age across all tissues (Fig. 6c and Supplementary Table 8, Benjamini–Hochberg adjusted *P* value < 0.02). This suggests a strong benefit of these coding reversion substitutions in ALR and FVB strains. In contrast, in NZB we observed an overwhelming preference for reversion alleles to decrease in frequency with age, particularly in the brain

(Fig. 6c and Supplementary Table 8). One potential explanation for this decrease in frequency compared with ALR and FVB is that the many NZB fixed substitutions exhibit epistatic interactions that manifest negatively if single reversions are not accompanied by mutations at other sites, though this is challenging to test. We did identify two cases in NZB of reversions that increase in frequency with age, a synonymous substitution in the *MT-CO2* gene, and a noncoding mutation in the *D-loop*. Together, our results demonstrate that sites which contribute to mito-nuclear mismatching are prone to elevated levels of mutation with reversion alleles preferred across multiple tissues in populations. This preference for nuclear mitochondrial matching potentially drives somatic selection increasing the frequency of these alleles with age.

## Discussion

The interdependence of nuclear- and mitochondrially encoded genes has shaped patterns of diversity and constraint on these two genomes across organisms and populations. Yet, the mt-genome also exhibits exceptionally high somatic mutation rates and is thus dynamic within individuals’ lifespans. Here we explored the relationship between nuclear–mitochondrial ancestral matching and the accumulation of somatic mutations. Our results extended upon other works that employ highly sensitive duplex sequencing to characterize the mutational landscape of the mt-genome<sup>34–37</sup> and generated, to our knowledge, the largest mt-genome somatic mutational catalogue so far. We profiled 2.5 million mt-genomes across four conplastic mouse strains and the B6 wild type, with a median of more than 74,000 mt-genomes per biological condition. Our results corroborated other studies of somatic mutation in the mt-genomes of mice, humans and macaques, which demonstrate an age-associated increase in mutations as well as tissue-specific mutation rates. Our study design also uniquely allowed us to assess the role of mt-haplotype on mutation rates. The conplastic strains employed each exhibit distinct physiological differences that probably play a role in modulating mutations. We find cases where mt-haplotype impacts mitochondrial mutation rate, which emphasizes that specific fixed substitutions between mt-haplotypes can play a vital role in shaping mutational profiles.

Our study design allows us to compare mutational landscapes across three of the most metabolically active tissues: the brain, heart and liver. We show that SNV mutation rates are haplotype and tissue specific. We also noted that, while most mutations increase in frequency with age, ROS-associated mutations do not. These findings recapitulate prior studies conducted by Arbeithuber et al.<sup>35</sup> and Sanchez-Contreras et al.<sup>37</sup>. Several hypotheses have been proposed to explain this phenomenon ranging from potential molecular mechanisms that recognize and remove ROS damage through ageing<sup>37</sup> to the existence of mitochondrial subpopulations that dictate the replication of specific, mutation-limited mtDNA molecules<sup>52,53</sup>. Further work is needed to identify the ultimate mechanisms that result in such non-clocklike signatures.

Our high duplex coverage allowed us to characterize mutational hotspots throughout the mt-genome at fine-scale resolution. As expected, the *D-loop* had a high mutation frequency compared with other regions in the genome. However, we identified three additional hotspots exhibiting either age- or haplotype-associated mutation frequencies. The first of these hotspots occurs in the *OrilL*, the light strand origin of replication, which forms a DNA stem–loop structure. While the sequence of this region is highly divergent among species, the structure is conserved. Recently, Arbeithuber et al.<sup>36</sup> identified the *OrilL* as a hotspot of mutation in macaque liver. We were also able to capture these hotspots in a re-analysis of recently published duplex sequencing data from several different tissues, despite their relatively lower sequencing coverage (Supplementary Fig. 11a,b and Supplementary Table 9)<sup>37</sup>. Similarly to Arbeithuber et al.<sup>36</sup>, we find mutations at the *OrilL* locus to be most prominent in aged wild-type liver, but our increased sequencing depth allows us to show that this is a consistent

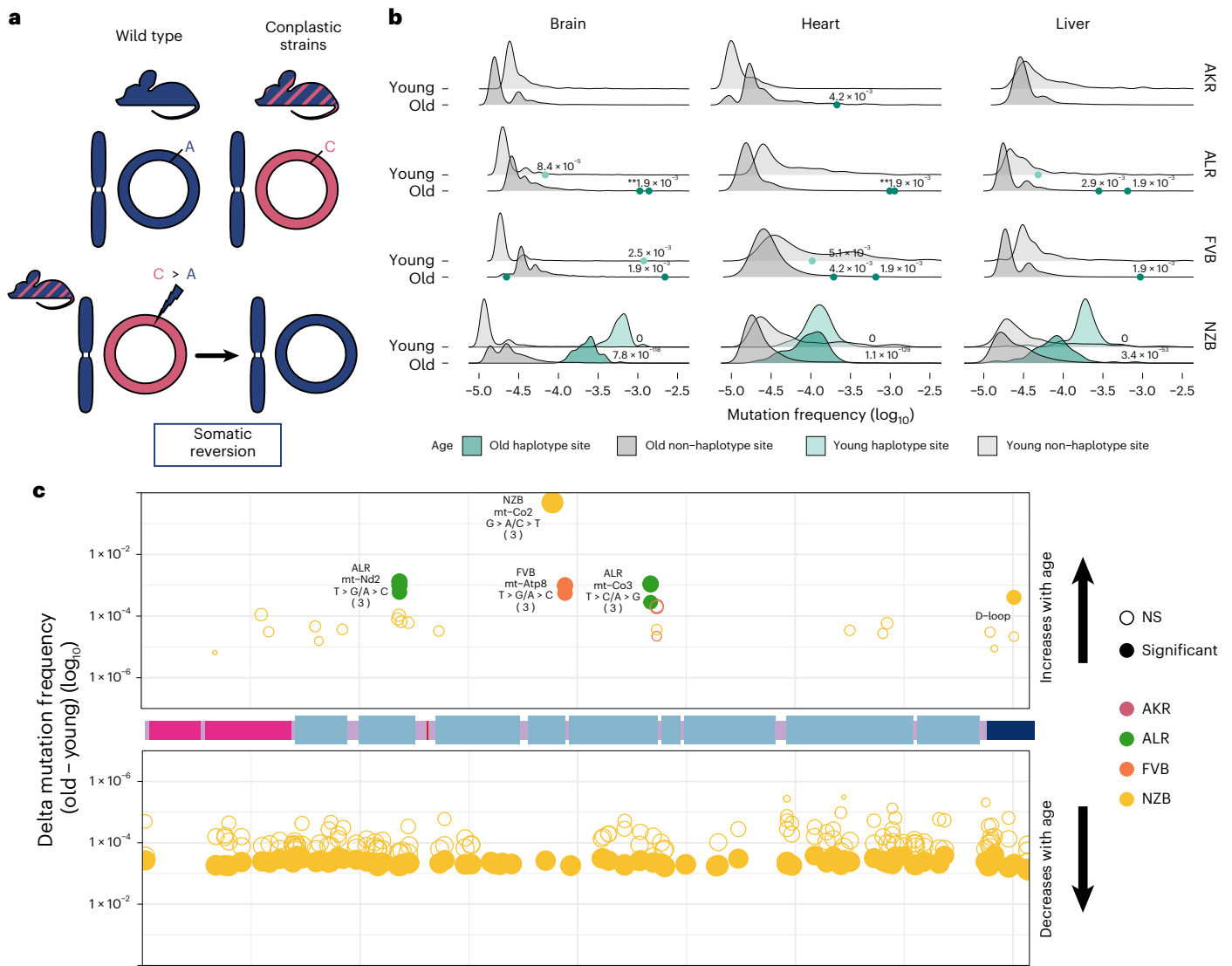


**Fig. 6 | Somatic reversion mutations segregate in the mt-genome population.** **a**, A schematic that explains somatic reversion mutations. The wild-type strain (B6) has matching nuclear and mt-genome ancestries (B6 ancestry denoted in blue). Conplastic strains are hybrids with mismatching nuclear and mt-genome ancestry. Haplotype sites are positions in the mt-genome where the conplastic mt-genome differs from the B6 mt-genome. Somatic reversion mutations refer to the re-introduction of B6 ancestral alleles at haplotype sites. **b**, The mutation frequency at non-haplotype sites (grey distributions) is compared with the mutation frequency at haplotype sites (green distributions or points when fewer than three haplotype sites exist). All mutations were included in the distribution of non-haplotype site mutation frequencies, including positions with a mutation frequency greater than  $1 \times 10^{-3}$ . Haplotype site mutation frequencies were corrected for potential NUMT contamination. Mutation frequencies were normalized for sequencing depth between young and aged experimental conditions. Denoted are the adjusted empirical  $P$  value using the Benjamini–Hochberg correction. Asterisks denote the

number of haplotype sites with the same  $P$  value. For AKR, ALR and FVB empirical  $P$  values for haplotype sites were calculated as the count of non-haplotype sites with a higher frequency than the haplotype site divided by the total number of non-haplotype sites (one-sided test). For NZB, the distribution of mutation frequencies for haplotype sites and non-haplotype sites was compared using the Wilcoxon rank-sum test. **c**, A map of the somatic reversion mutations along a linear mt-genome. Each point denotes the change in frequency with age (delta) for a somatic reversion mutation. The size of the point indicates the magnitude of delta and colour represents the conplastic strain the somatic reversion occurs in. Empirical  $P$  values were calculated as the count of sites with a delta greater (for sites with an increase in frequency with age) or less (for sites with a decrease in frequency with age) than the haplotype site delta divided by the total number of deltas (one-sided test). Fill denotes significance: not significant (NS) in hollow points and significant in filled points (adjusted empirical  $P$  value  $< 0.02$  using the Benjamini–Hochberg correction within each mt-haplotype group).

hotspot across tissues and strains regardless of age. We identify mutations in both the stem and the loop of this structure, with mutations occurring in the same 5' end of the stem as those identified in macaque, albeit impacting completely different sequences. We further noted that there is a well-supported mechanism for this specific mutational hotspot occurring on one arm of the stem–loop structure due to replication priming by an RNA that is susceptible to slippage<sup>54</sup>. These results highlight that the conserved structure of this stem–loop is sensitizing to conserved mutational patterns across species. Similarly, peaks of mutation frequency within the *D-loop* have been narrowed to regions

associated with mtDNA replication<sup>20,51,55</sup>. The mutational hotspots surrounding mtDNA origins of replication have been hypothesized to serve as a compensatory mechanism against mutation by slowing mtDNA replication<sup>36</sup>. We identified an additional hotspot occurring in a highly structured nucleic acid, *MT-tRNA<sup>Arg</sup>*. Intriguingly, these mutations are only found in conplastic strains, suggesting that they are poorly tolerated in the wild type. These mutations are expected to increase the size of the loop in the 5' D-arm stem–loop of this tRNA. Polymorphisms that increase the size of the D-arm in *MT-tRNA<sup>Arg</sup>* have been linked with an increase in mtDNA copy number triggered by

heightened ROS production<sup>56</sup>. Specifically, the size of the loop, not the underlying sequence, was found to be important for mitochondrial function<sup>43</sup>. Together, these findings suggest that mutational hotspots in the mt-genome may potentially act as compensatory mechanisms to alter mtDNA replication and copy number.

While duplex sequencing approaches have allowed us to identify processes associated with DNA replication as the primary driver of somatic mutations in mitochondria<sup>34–36</sup>, the full extent of mutational processes impacting mt-genomes remains unknown. Recent studies have determined that different species exhibit varying contributions of mutational signatures in the nuclear genomes of ageing intestinal crypt cells<sup>49</sup>. Comparing the mutational spectra across several studies that duplex sequence the mt-genomes of humans, mice and macaques in various tissues, we similarly find that rodents exhibit distinct mutational profiles compared with primates. Although DNA replication error is the predominant mutation type across species, rodents exhibit a surfeit of G > T mutations in contrast to primates. While studies in humans previously concluded that transitions are the most common mutation in mitochondria, we find that the abundance of the T > C marker of DNA replication error is a species-specific effect. We are not able to determine whether this finding is the result of physiological differences between these organisms, or variability in the repair pathways of these species. Of note, we find these trends hold both for somatic mutations as well as de novo oocyte mutations in the mt-genome, suggesting that the underlying mechanisms driving these distinct profiles have potentially shaped patterns of mitochondrial diversity across different species. Intriguingly, a very similar signature distinguishing mice and ferrets from other mammals was found using laser-capture and deep sequencing of intestinal crypts across 16 species<sup>49</sup>. Together, these findings thus recapitulate that distinct life history traits impact the evolution of the mt-genome across species. Compared with primates, rodents have a shorter lifespan and a substantially smaller body size. The difference in G > T mutations, which are associated with ROS damage, and T > C mutations, a marker of DNA replication error, suggest that repair mechanisms or ROS defenses may differ between these species. Further analyses across broad ranges of species, such as those recently performed in the nuclear genome<sup>49</sup>, are needed to inform how mitochondrial mutational processes are specifically associated with disparate life histories.

Mitochondrial genomes exist as a population inside cells, where selection can act to shape this population at various biological scales. In oocytes, strong genetic drift induced by the mitochondrial genetic bottleneck<sup>26</sup> and purifying selection<sup>20,57</sup> have been shown to shape the transmission of mt-genome mutations across generations. In somatic tissues, the population of mt-genomes may be shaped at the cellular level, as a result of inter-cellular competition; at the inter-mitochondrial level, with mitochondrial turnover; or at the intra-mitochondrial level between mt-genomes harbouring different variants. Previous studies focused on de novo mutations in mice have not identified signals of selection<sup>35,37</sup>. However, it has been suggested that this may be due to the low frequencies of these variants, which prevents them from having a phenotypic effect on mitochondrial function. By contrast, studies focused on higher-frequency mutations in humans (greater than 0.5% frequency) have identified signals of positive selection<sup>51</sup>, and potential signals of negative selection<sup>51,58</sup> based on differences between polymorphic and heteroplasmic non-synonymous mutations. Furthermore, signatures of positive selection in the liver have been previously reported in both macaques<sup>36</sup> and humans<sup>51</sup>. Complementing these studies, we find that low-frequency mutations, which are probably de novo somatic mutations, are not under strong selection. However, mutations at intermediate frequencies, ranging from  $5 \times 10^{-5}$  to  $1 \times 10^{-3}$ , do exhibit some signatures of negative selection. While these are probably not de novo mutations, they demonstrate a low frequency threshold for tissue-specific selection of inherited or early developmental mutations. Importantly, our results demonstrate that

mitochondrial mutational spectra vary across different frequencies and mutational hotspots (Fig. 5b), which can influence signatures of selection. Together, these findings suggest that purifying selection acts on mitochondrial mutations segregating at lower frequencies.

Our study also allowed us to examine a very specific form of somatic selection: the emergence and persistence of reversion mutations that re-match the mt-haplotype to its nuclear constituent. Previously, Wei et al. identified the preferred maternal transmission of de novo variants that worked to re-align mitochondrial and nuclear ancestry in humans<sup>20</sup>. This result showcased that selection for reversions can occur in as short as one generation, emphasizing the strong influence mito-nuclear interactions have in shaping mt-genome diversity. We find selection for reversion mutations at even shorter time-scales: within an organism's lifespan. These mutations are extremely abundant, much more than expected by chance, and in several cases increase in frequency with age. Importantly, the change in reversion allele frequencies with age was dependent on the genetic divergence between the mitochondrial and nuclear ancestries. That is, mice with the greatest genetic divergence from the B6-mt-haplotype observed the opposite trend, a decrease in reversion frequency with age. Despite mito-nuclear ancestral mismatching, NZB mice did not showcase phenotypic differences compared to B6 (ref. 59). Thus, understanding to what extent mito-nuclear matching influences somatic evolution remains to be explored. Altogether, these observations highlight a hitherto unexplored impact of mito-nuclear incompatibility, namely its potential role on the somatic evolution of tissues.

While we sequence to great depth across various tissues, we are unable to characterize the impact that cell type plays on the evolution of the mt-genome. This analysis is of particular interest in tissues such as the heart and the brain that consist of both mitotic and post-mitotic cellular populations. Given that DNA replication error is a predominant age-associated mutational signature, sequencing at the single-cell level will be pivotal in understanding the role that cell proliferation has on mitochondrial somatic mutation. Additionally, our study only examined the wild-type B6 mouse and conplastic strains with nuclear B6 backgrounds. Reciprocal conplastic strains, in which both mt-haplotypes are placed in the context of both nuclear genomes, will allow us to parse apart the different roles that the nuclear and mitochondrial genomes have in driving distinct mutational processes. Lastly, our study emphasizes the importance of comparative somatic mutation profiling to discern how processes that shape mutation in the mt-genome differ with life history traits. Altogether, our findings explore somatic evolution in the context of an important cellular organelle and begin to discern the various scales at which evolutionary processes act to shape the population of mt-genomes.

## Methods

### Ethics statement

Animal use and all methods were approved by the Animal Care and Use Committee (V242-7224. 122-5, Kiel, Germany). Experiments were performed in accordance with the relevant guidelines and regulations by certified personnel.

### Data collection and sample preparation

The wild-type C57BL/6J (B6) and inbred mouse strains were obtained from Jackson Laboratory and maintained at the University of Lübeck. Conplastic strains B6-mtAKR, B6-mtALR, B6-mtFVB and B6-mtNZB were generated and bred as described in ref. 38 at the University of Lübeck. Briefly, the conplastic strains were developed by crossing female mice from AKR, ALR, FVB and NZB mouse strains with male B6 mice. Female offspring were then backcrossed with male B6 mice. After the tenth generation of backcrossing, mice were deemed conplastic mice with a B6 nuclear background and their respective maternal mt-haplotypes. Samples were validated by checking for their defining haplotype sites (Supplementary Table 1 and Supplementary Fig. 12). The brain,

heart and liver were sampled from young (2–4 months old) and aged (15–22 months old) mice in each strain ( $n = 115$ ). B6 young liver samples and one B6 young heart sample were omitted from the data due to possible contamination (Supplementary Fig. 12). Whole tissue samples were flash frozen and processed for DNA isolation using the Qiagen DNAeasy Blood and Tissue kit (ID: 69504). All mice in this study are female.

### Sequencing

Duplex sequencing libraries were prepared by TwinStrand Biosciences as previously described<sup>33,34</sup>. Sequencing was performed at the University of California, Berkeley using Illumina NovaSeq generated 150-bp paired-end reads.

### Data processing

Sequencing reads were processed into duplex sequencing reads and mapped to the reference mouse mt-genome (mm10) using a modified version of the duplex sequencing processing pipeline developed by Dr Scott Kennedy's group at the University of Washington, Seattle. The pipeline was edited to take as input bam files formed from the NovaSeq reads using `bwa mem`<sup>60</sup> and `samtools`<sup>61</sup>, and is available on our GitHub. Software versions used along with all processing steps including duplex consensus sequencing generation, mapping and variant calling can be found in the GitHub repository referenced below. Parameters used to run the duplex sequencing pipeline are provided in Supplementary Note 1.

### Trinucleotide spectra

Only de novo mutations were used in this analysis and were identified by filtering for mutations with an alternative allele depth <100 and a mutation frequency <0.01. Each mutation is scored once to create a proxy mutation frequency for de novo mutations. The mutation fraction is the proportion of each mutation type in a given trinucleotide context divided by the total count of de novo mutations for a condition. The trinucleotide and mutation type featured represent mutations on either strand. For example, in the C > T/G > A facet ACG represents both ACG and CGT, where either a C > T or a G > A mutation has occurred (Supplementary Fig. 13).

### Mutational signature extraction

Observed counts for each mutation type (excluding mutations at a frequency > $1 \times 10^{-3}$ ) were used as input for `sigfit` (v 2.2), which is an R package used to identify mutational signatures. `Sigfit` uses Bayesian probabilistic modelling to uncover mutational signatures, as explained by Gori and Baez-Ortega<sup>48</sup>. Specifically, we use multinomial models to extract our signatures, which is akin to the traditional non-negative matrix factorization approaches. The optimal number of signatures was determined by extracting a range of one to seven signatures and comparing the cosine similarity (Supplementary Fig. 8) for this range (iterations 1,000, seed 1,756). The model was then refitted with two signatures, as determined by the goodness of fit test, with 10,000 iterations (seed 1,756).

### Testing for selection

The number of non-synonymous variants per non-synonymous sites (hN) and synonymous variants per synonymous sites (hS) were calculated as described in refs. 35,51.

We quantified mutations and mutation type proportions in three different ways: (1) all mutations, without consideration of mutation frequency or mt-genome position (2) all mutations excluding the *D-loop* (3) mutation counts binned by mutation frequency, excluding the *D-loop*. Mutation counts were calculated as the sum of the duplex alternative allele depth across all sites in the mt-genome. Counts were aggregated across replicates in experimental conditions (Supplementary Fig. 14a).

For analyses where mutation counts were aggregated across frequencies, the  $\frac{hN}{hS}$  statistic was quantified for each gene across the 29 experimental conditions. To test if the observed  $\frac{hN}{hS}$  statistics were

significant signals of selection, we used a multinomial distribution to simulate mutations for all experimental conditions using the observed mutation counts and proportions for each mutation type. The mutations were sampled across the mt-genome uniformly with replacement, and the simulated  $\frac{hN}{hS}$  statistics were calculated for each gene. A total of 10,000 simulations were conducted for each experimental condition.  $\frac{hN}{hS}$  statistics that could not be calculated (hS of 0 or hN of 0) were excluded from the analysis. Mutations with a frequency > $1 \times 10^{-3}$  were excluded from these analyses. Empirical  $P$  values were used to determine if an observed  $\frac{hN}{hS}$  statistic was significant. The empirical  $P$  value was calculated as the number of simulated  $\frac{hN}{hS}$  statistics with a more extreme value than the observed  $\frac{hN}{hS}$  statistic divided by the total number of simulated statistics. These empirical  $P$  values were multiplied by a factor of 2 to account for both tails of the distribution.  $\frac{hN}{hS}$  statistics with a Benjamini–Hochberg adjusted  $P$  values <0.01 were denoted as significant, where  $\frac{hN}{hS} > 1$  signified that a gene was under positive selection and  $\frac{hN}{hS} < 1$  suggested a gene was under negative selection.

For analyses where mutation counts were binned by frequencies, mutations with a frequency > $1 \times 10^{-3}$  were included.  $\frac{hN}{hS}$  statistics were calculated for each bin across every experimental condition. Mutation counts were calculated as the sum of the duplex alternative allele depth across all sites in the mt-genome within the frequency bin. Counts were aggregated across replicates in experimental conditions. The analysis described above was performed for every bin in each experimental condition. A Benjamini–Hochberg multiple hypothesis test correction was applied for each bin to maintain consistency in the number of tests corrected for between the aggregated and binned analyses. The proportion of genes under selection for each analysis is shown in Supplementary Fig. 14b.

### Comparison of the null and observed mutational spectra for non-synonymous and synonymous mutations

The null mutational spectra for synonymous and non-synonymous mutations were calculated by quantifying the number of non-synonymous and synonymous mutations each mutation type could produce. The proportion was calculated as the count of non-synonymous or synonymous mutations resulting from a given mutation type divided by all possible non-synonymous or synonymous mutations in the mt-genome (Supplementary Fig. 15a). For the observed mutational spectra, the proportion of each mutation type comprising the total count of non-synonymous and synonymous mutations was calculated (Supplementary Fig. 15b).

### Estimation of and correction for NUMT contamination

We originally mapped duplex paired end reads to the mm10 reference genome masking the known nuclear mitochondrial DNA segment (NUMT) region in chromosome 1. We reasoned that, given the 10–100-fold higher somatic mutation rate of the mt-genome along with its several-hundred fold increased copy number with respect to the nuclear genome, nuclear contaminating reads contribute minimally to our mutation frequencies. However, this low-level of contamination can potentially cause an issue when examining reversion mutations that are expected to be enriched for the B6 allele in the NUMT.

To estimate and correct for this NUMT contamination, duplex paired end reads were remapped to mm10 using 'bwa mem'. For this remapping, the NUMT region in chr1 (nt24611535 to nt246116184) was unmasked. The duplex read depth at junction regions, which captured sequences 10 bp upstream and 10 bp downstream of the NUMT region in chr1 and the corresponding region in the mt-genome (nt6394 to nt11042), was calculated using `samtools depth {input.in1} -b {input.in2} > {output}`. These junction regions contain sequences unique to chr1 and chrM, allowing us to estimate the percentage of reads mapping to chr1 as the number of reads mapping to chr1 divided by the average duplex depth of the mt-genome calculated with the chr1 NUMT masked (Supplementary Fig. 16a).

To validate this estimated contamination, we remapped the duplex paired end reads to the NZB reference genome (generated using an in-house script). The NZB mt-genome and B6 NUMT region differ by 24 SNVs. To map the duplex reads to the NUMT region we used samtools depth {input.in1} -bq 30 {input.in2} > {output}, setting a strict mapping quality score given that reads may differ from the regions by as few as two positions. Six regions across the NUMT were identified as having multiple SNVs within a read (<130 bp apart), which we refer to as SNV clusters. We used these clusters to identify reads that mapped to chr1. The estimated percentage of NUMT contamination at each SNV cluster was calculated as the number of reads mapping to chr1 divided by the average duplex depth of the mt-genome calculated with the chr1 NUMT masked. The estimated percentage of contamination at the junction regions was compared with the distribution of estimated percentage of contamination for the SNV clusters in NZB (Supplementary Fig. 16b). The maximum estimated percentage of contamination between the junction regions was consistently equal to the median estimated percentage of contamination for the SNV clusters in NZB, verifying the consistency of the estimated percentage of NUMT contamination.

We take as a conservative measure the maximum estimated percentage of contamination from the junction regions (~0.5% contamination). The estimated chr1 read depth was then calculated as the original average mt-genome duplex depth multiplied by the estimated percentage of contamination. We calculated the corrected duplex mt-genome read depth in this region as the original duplex mt-genome read depth subtracted by the estimated chr1 read depth count. Likewise, the reversion allele depth is calculated as the original reversion allele count subtracted by the estimated chr1 read depth, assuming all reads from chr1 contain the B6 allele.

### Statistical analysis: testing for significance

Statistical analyses were performed using R (4.1.2). Poisson confidence intervals for average mutation frequencies were calculated using the qchisq function from the stats package in R (v 4.1.2). log-link regressions were performed to determine an age-associated change in mutation frequency and mt-haplotype specific mutation rates (glm, stats package). Associations between (1) mutation type and age and (2) reversion allele and haplotype site were determined via Fisher's exact tests (fisher.test, stats package). To compare the average mutation frequencies between the D-loop and other regions in the mt-genome we used two tailed *t*-tests (t.test, stats package). To compare background to haplotype site mutation frequencies for the NZB conplastic strain, we conducted Wilcoxon rank-sum tests (wilcoxon.test, stats package). Lastly, we calculate empirical *P* values to determine the significance of observed  $\frac{h_N}{h_S}$  statistics; high haplotype site mutation frequencies for AKR, ALR and FVB; and for changes in mutation frequency with age for all haplotype sites. The empirical *P* values are calculated as the number of simulated  $\frac{h_N}{h_S}$  statistic (for 1) or number of background sites (for 2 and 3) with a more extreme value than our observed  $\frac{h_N}{h_S}$  statistic (for 1), haplotype site mutation frequency (for 2), or change in mutation frequency for the haplotype site (for 3), divided by the total number of simulations (for 1) or total number of background sites (for 2 and 3). Multiple hypothesis test corrections were performed using the Bonferroni or Benjamini–Hochberg correction (p.adjust, stats package), adjusted *P* values refer to *P* values that have undergone multiple hypothesis correction.

### Reporting summary

Further information on research design is available in the Nature Portfolio Reporting Summary linked to this article.

### Data availability

All raw data have been uploaded to Sequence Read Archive (SRA Bio-Project ID: PRJNA1054208). Single-stranded consensus and duplex consensus sequences, and processed data, have been deposited in Zenodo.

The Zenodo repository can be accessed at <https://doi.org/10.5281/zenodo.7787188>.

### Code availability

All code has been deposited in GitHub ([https://github.com/sudmant-lab/conplastic\\_mt\\_profiling](https://github.com/sudmant-lab/conplastic_mt_profiling)) with the repository archived in Zenodo at <https://doi.org/10.5281/zenodo.10360087>.

### References

- Hill, G. E. Mitonuclear compensatory coevolution. *Trends Genet.* **36**, 403–414 (2020).
- Osada, N. & Akashi, H. Mitochondrial–nuclear interactions and accelerated compensatory evolution: evidence from the primate cytochrome C oxidase complex. *Mol. Biol. Evol.* **29**, 337–346 (2012).
- Barreto, F. S. & Burton, R. S. Evidence for compensatory evolution of ribosomal proteins in response to rapid divergence of mitochondrial rRNA. *Mol. Biol. Evol.* **30**, 310–314 (2013).
- Weaver, R. J., Rabinowitz, S., Thueson, K. & Havird, J. C. Genomic signatures of mitonuclear coevolution in mammals. *Mol. Biol. Evol.* **39**, msac233 (2022).
- Montooth, K. L., Meiklejohn, C. D., Abt, D. N. & Rand, D. M. Mitochondrial–nuclear epistasis affects fitness within species but does not contribute to fixed incompatibilities between species of *Drosophila*. *Evolution* **64**, 3364–3379 (2010).
- Meiklejohn, C. D. et al. An incompatibility between a mitochondrial tRNA and its nuclear-encoded tRNA synthetase compromises development and fitness in *Drosophila*. *PLoS Genet.* **9**, e1003238 (2013).
- Ellison, C. K. & Burton, R. S. Disruption of mitochondrial function in interpopulation hybrids of *Tigriopus californicus*. *Evolution* **60**, 1382–1391 (2006).
- Ellison, C. K. & Burton, R. S. Interpopulation hybrid breakdown maps to the mitochondrial genome. *Evolution* **62**, 631–638 (2008).
- Niehuis, O., Judson, A. K. & Gadau, J. Cytonuclear genic incompatibilities cause increased mortality in male F2 hybrids of *Nasonia giraulti* and *N. vitripennis*. *Genetics* **178**, 413–426 (2008).
- Ellison, C. K., Niehuis, O. & Gadau, J. Hybrid breakdown and mitochondrial dysfunction in hybrids of *Nasonia parasitoid* wasps. *J. Evol. Biol.* **21**, 1844–1851 (2008).
- Koevoets, T., Niehuis, O., van de Zande, L. & Beukeboom, L. W. Hybrid incompatibilities in the parasitic wasp genus *Nasonia*: negative effects of hemizygoty and the identification of transmission ratio distortion loci. *Heredity* **108**, 302–311 (2012).
- Lee, H.-Y. et al. Incompatibility of nuclear and mitochondrial genomes causes hybrid sterility between two yeast species. *Cell* **135**, 1065–1073 (2008).
- Chou, J.-Y., Hung, Y.-S., Lin, K.-H., Lee, H.-Y. & Leu, J.-Y. Multiple molecular mechanisms cause reproductive isolation between three yeast species. *PLoS Biol.* **8**, e1000432 (2010).
- Morales, H. E. et al. Concordant divergence of mitogenomes and a mitonuclear gene cluster in bird lineages inhabiting different climates. *Nat. Ecol. Evol.* **2**, 1258–1267 (2018).
- Moran, B. M. et al. A lethal mitonuclear incompatibility in complex I of natural hybrids. *Nature* **626**, 119–127 (2024).
- Baris, T. Z. et al. Evolved genetic and phenotypic differences due to mitochondrial–nuclear interactions. *PLoS Genet.* **13**, e1006517 (2017).
- Ellison, C. K. & Burton, R. S. Cytonuclear conflict in interpopulation hybrids: the role of RNA polymerase in mtDNA transcription and replication. *J. Evol. Biol.* **23**, 528–538 (2010).
- Ellison, C. K. & Burton, R. S. Genotype-dependent variation of mitochondrial transcriptional profiles in interpopulation hybrids. *Proc. Natl Acad. Sci. USA* **105**, 15831–15836 (2008).

19. Zaidi, A. A. & Makova, K. D. Investigating mitonuclear interactions in human admixed populations. *Nat. Ecol. Evol.* **3**, 213–222 (2019).
20. Wei, W. et al. Germline selection shapes human mitochondrial DNA diversity. *Science* **364**, aau6520 (2019).
21. Jenuth, J. P., Peterson, A. C. & Shoubridge, E. A. Tissue-specific selection for different mtDNA genotypes in heteroplasmic mice. *Nat. Genet.* **16**, 93–95 (1997).
22. Battersby, B. J. & Shoubridge, E. A. Selection of a mtDNA sequence variant in hepatocytes of heteroplasmic mice is not due to differences in respiratory chain function or efficiency of replication. *Hum. Mol. Genet.* **10**, 2469–2479 (2001).
23. Battersby, B. J., Loredó-Ostí, J. C. & Shoubridge, E. A. Nuclear genetic control of mitochondrial DNA segregation. *Nat. Genet.* **33**, 183–186 (2003).
24. López-Otín, C., Blasco, M. A., Partridge, L., Serrano, M. & Kroemer, G. The hallmarks of aging. *Cell* **153**, 1194–1217 (2013).
25. Jónsson, H. et al. Parental influence on human germline de novo mutations in 1,548 trios from Iceland. *Nature* **549**, 519–522 (2017).
26. Rebolledo-Jaramillo, B. et al. Maternal age effect and severe germ-line bottleneck in the inheritance of human mitochondrial DNA. *Proc. Natl Acad. Sci. USA* **111**, 15474–15479 (2014).
27. Linnane, A. W., Marzuki, S., Ozawa, T. & Tanaka, M. Mitochondrial DNA mutations as an important contributor to ageing and degenerative diseases. *Lancet* [https://doi.org/10.1016/s0140-6736\(89\)92145-4](https://doi.org/10.1016/s0140-6736(89)92145-4) (1989).
28. Bogenhagen, D. & Clayton, D. A. The number of mitochondrial deoxyribonucleic acid genomes in mouse l and human HeLa Cells: quantitative isolation of mitochondrial deoxyribonucleic acid. *J. Biol. Chem.* **249**, 7991–7995 (1974).
29. Filograna, R., Mennuni, M., Alsina, D. & Larsson, N.-G. Mitochondrial DNA copy number in human disease: the more the better? *FEBS Lett.* **595**, 976–1002 (2021).
30. Sanchez-Contreras, M. & Kennedy, S. R. The complicated nature of somatic mtDNA mutations in aging. *Front. Aging* **2**, 805126 (2022).
31. López-Otín, C., Blasco, M. A., Partridge, L., Serrano, M. & Kroemer, G. Hallmarks of aging: an expanding universe. *Cell* <https://doi.org/10.1016/j.cell.2022.11.001> (2022).
32. Wallace, D. C. Mitochondrial diseases in man and mouse. *Science* **283**, 1482–1488 (1999).
33. Schmitt, M. W. et al. Detection of ultra-rare mutations by next-generation sequencing. *Proc. Natl Acad. Sci. USA* **109**, 14508–14513 (2012).
34. Kennedy, S. R., Salk, J. J., Schmitt, M. W. & Loeb, L. A. Ultra-sensitive sequencing reveals an age-related increase in somatic mitochondrial mutations that are inconsistent with oxidative damage. *PLoS Genet.* **9**, e1003794 (2013).
35. Arbeithuber, B. et al. Age-related accumulation of de novo mitochondrial mutations in mammalian oocytes and somatic tissues. *PLoS Biol.* **18**, e3000745 (2020).
36. Arbeithuber, B. et al. Advanced age increases frequencies of de novo mitochondrial mutations in macaque oocytes and somatic tissues. *Proc. Natl Acad. Sci. USA* **119**, e2118740119 (2022).
37. Sanchez-Contreras, M. et al. The multi-tissue landscape of somatic mtDNA mutations indicates tissue specific accumulation and removal in aging. *eLife* **12**, e83395 (2023).
38. Yu, X. et al. Dissecting the effects of mtDNA variations on complex traits using mouse conplastic strains. *Genome Res.* **19**, 159–165 (2009).
39. Abascal, F. et al. Somatic mutation landscapes at single-molecule resolution. *Nature* **593**, 405–410 (2021).
40. Wanrooij, S. et al. In vivo mutagenesis reveals that OriL is essential for mitochondrial DNA replication. *EMBO Rep.* **13**, 1130–1137 (2012).
41. Laslett, D. & Canbäck, B. ARWEN: a program to detect tRNA genes in metazoan mitochondrial nucleotide sequences. *Bioinformatics* **24**, 172–175 (2008).
42. Quigley, G. J. & Rich, A. Structural domains of transfer RNA molecules. *Science* **194**, 796–806 (1976).
43. Moreno-Loshuertos, R., Pérez-Martos, A., Fernández-Silva, P. & Enriquez, J. A. Length variation in the mouse mitochondrial tRNA(Arg) DHU loop size promotes oxidative phosphorylation functional differences. *FEBS J.* **280**, 4983–4998 (2013).
44. Alexandrov, L. B. et al. Signatures of mutational processes in human cancer. *Nature* **500**, 415–421 (2013).
45. Duncan, B. K. & Miller, J. H. Mutagenic deamination of cytosine residues in DNA. *Nature* **287**, 560–561 (1980).
46. Zheng, W., Khrapko, K., Coller, H. A., Thilly, W. G. & Copeland, W. C. Origins of human mitochondrial point mutations as DNA polymerase gamma-mediated errors. *Mutat. Res* **599**, 11–20 (2006).
47. Cheng, K. C., Cahill, D. S., Kasai, H., Nishimura, S. & Loeb, L. A. 8-Hydroxyguanine, an abundant form of oxidative DNA damage, causes G–T and A–C substitutions. *J. Biol. Chem.* **267**, 166–172 (1992).
48. Gori, K. & Baez-Ortega, A. sigfit: flexible Bayesian inference of mutational signatures. Preprint at *bioRxiv* <https://doi.org/10.1101/372896> (2020).
49. Cagan, A. et al. Somatic mutation rates scale with lifespan across mammals. *Nature* **604**, 517–524 (2022).
50. Williams, S. L., Mash, D. C., Züchner, S. & Moraes, C. T. Somatic mtDNA mutation spectra in the aging human putamen. *PLoS Genet.* **9**, e1003990 (2013).
51. Li, M., Schröder, R., Ni, S., Madea, B. & Stoneking, M. Extensive tissue-related and allele-related mtDNA heteroplasmy suggests positive selection for somatic mutations. *Proc. Natl Acad. Sci. USA* **112**, 2491–2496 (2015).
52. Cote-L'Heureux, A. et al. The ‘Stem’ and the ‘Workers’ of the mtDNA population of the cell. Evidence from mutational analysis. Preprint at *bioRxiv* <https://doi.org/10.1101/2023.04.14.536897> (2023).
53. Cote-L'Heureux, A., Maithania, Y. N. K., Franco, M. & Khrapko, K. Are some mutations more equal than others? *eLife* **12**, e87194 (2023).
54. Sarfallah, A., Zamudio-Ochoa, A., Anikin, M. & Temiakov, D. Mechanism of transcription initiation and primer generation at the mitochondrial replication origin OriL. *EMBO J.* **40**, e107988 (2021).
55. Samuels, D. C. et al. Recurrent tissue-specific mtDNA mutations are common in humans. *PLoS Genet.* **9**, e1003929 (2013).
56. Moreno-Loshuertos, R. et al. Differences in reactive oxygen species production explain the phenotypes associated with common mouse mitochondrial DNA variants. *Nat. Genet.* **38**, 1261–1268 (2006).
57. Zaidi, A. A. et al. Bottleneck and selection in the germline and maternal age influence transmission of mitochondrial DNA in human pedigrees. *Proc. Natl Acad. Sci. USA* **116**, 25172–25178 (2019).
58. Li, M. et al. Detecting heteroplasmy from high-throughput sequencing of complete human mitochondrial DNA genomes. *Am. J. Hum. Genet.* **87**, 237–249 (2010).
59. Hirose, M. et al. Lifespan effects of mitochondrial mutations. *Nature* **540**, E13–E14 (2016).
60. Li, H. Aligning sequence reads, clone sequences and assembly contigs with BWA-MEM. Preprint at <https://doi.org/10.48550/arXiv.1303.3997> (2013).
61. Danecek, P. et al. Twelve years of SAMtools and BCFtools. *Gigascience* **10**, giab008 (2021).

## Acknowledgements

Institute of General Medical Sciences (grant: R35GM142916) to P.H.S. Vallee Scholars Award to P.H.S. Glenn Foundation for Medical Research and AFAR Grant for Junior Faculty to P.H.S. Shurl and Kay Curci Foundation Grant to P.H.S. National Science Foundation Graduate Student Fellowship (grant: DGE 1752814; DGE 2146752), University of California, Berkeley Graduate Fellowship, the Rose Hills Foundation Fellowship, and the Ford Foundation Dissertation Fellowship to I.M.S.

## Author contributions

Conceived the experimental design: P.H.S. Constructed the conplastic strains and provided experimental samples: M.H. and S.I. Sequencing design and library preparation: C.C.V., S.R., E.S., G.P., L.W. and J.S. L.W. and G.P. contributed to this project while affiliated with TwinStrand Biosciences. Processed and analysed the data: I.M.S. and P.H.S. Wrote and edited the manuscript: I.M.S. and P.H.S.

## Competing interests

C.C.V., S.R., E.S., G.P., L.W. and J.S. declare they are equity holders of TwinStrand Biosciences, Inc. Additionally, C.C.V., E.S. and J.S. are current employees of TwinStrand Biosciences, and C.C.V., E.S., L.W. and J.S. are inventors on one or more duplex sequencing-related patents. All other authors declare no competing interests.

## Additional information

**Supplementary information** The online version contains supplementary material available at <https://doi.org/10.1038/s41559-024-02338-3>.

**Correspondence and requests for materials** should be addressed to Peter H. Sudmant.

**Peer review information** *Nature Ecology & Evolution* thanks Konstantin Khrapko, Kendra Zwonitzer and the other, anonymous, reviewer(s) for their contribution to the peer review of this work.

**Reprints and permissions information** is available at [www.nature.com/reprints](http://www.nature.com/reprints).

**Publisher's note** Springer Nature remains neutral with regard to jurisdictional claims in published maps and institutional affiliations.

**Open Access** This article is licensed under a Creative Commons Attribution 4.0 International License, which permits use, sharing, adaptation, distribution and reproduction in any medium or format, as long as you give appropriate credit to the original author(s) and the source, provide a link to the Creative Commons licence, and indicate if changes were made. The images or other third party material in this article are included in the article's Creative Commons licence, unless indicated otherwise in a credit line to the material. If material is not included in the article's Creative Commons licence and your intended use is not permitted by statutory regulation or exceeds the permitted use, you will need to obtain permission directly from the copyright holder. To view a copy of this licence, visit <http://creativecommons.org/licenses/by/4.0/>.

© The Author(s) 2024

## Reporting Summary

Nature Portfolio wishes to improve the reproducibility of the work that we publish. This form provides structure for consistency and transparency in reporting. For further information on Nature Portfolio policies, see our [Editorial Policies](#) and the [Editorial Policy Checklist](#).

### Statistics

For all statistical analyses, confirm that the following items are present in the figure legend, table legend, main text, or Methods section.

n/a | Confirmed

- The exact sample size ( $n$ ) for each experimental group/condition, given as a discrete number and unit of measurement
- A statement on whether measurements were taken from distinct samples or whether the same sample was measured repeatedly
- The statistical test(s) used AND whether they are one- or two-sided  
*Only common tests should be described solely by name; describe more complex techniques in the Methods section.*
- A description of all covariates tested
- A description of any assumptions or corrections, such as tests of normality and adjustment for multiple comparisons
- A full description of the statistical parameters including central tendency (e.g. means) or other basic estimates (e.g. regression coefficient) AND variation (e.g. standard deviation) or associated estimates of uncertainty (e.g. confidence intervals)
- For null hypothesis testing, the test statistic (e.g.  $F$ ,  $t$ ,  $r$ ) with confidence intervals, effect sizes, degrees of freedom and  $P$  value noted  
*Give  $P$  values as exact values whenever suitable.*
- For Bayesian analysis, information on the choice of priors and Markov chain Monte Carlo settings
- For hierarchical and complex designs, identification of the appropriate level for tests and full reporting of outcomes
- Estimates of effect sizes (e.g. Cohen's  $d$ , Pearson's  $r$ ), indicating how they were calculated

*Our web collection on [statistics for biologists](#) contains articles on many of the points above.*

### Software and code

Policy information about [availability of computer code](#)

Data collection	Raw illumina reads were processed into duplex reads using the publicly available duplex processing pipeline from the Kennedy Lab at the University of Washington, Seattle. The following software and versions are used in the pipeline: Python version: 3.7.3, Conda version: 4.7.12, Snakemake version: 5.10.0, BWA version 0.7.17-r1188, Pandas, a GATK3.8.1 .jar file, and wget.
Data analysis	Statistical analyses were performed using R (4.1.2) and relied on functions from the stats package (4.1.2). Simulations for the hN/hS ratio were conducted using Python (3.9.5) and the following packages: numpy (1.21.2), pandas (1.4.1), and SeqIO from biopython (1.78).

For manuscripts utilizing custom algorithms or software that are central to the research but not yet described in published literature, software must be made available to editors and reviewers. We strongly encourage code deposition in a community repository (e.g. GitHub). See the Nature Portfolio [guidelines for submitting code & software](#) for further information.



## Data

Policy information about [availability of data](#)

All manuscripts must include a [data availability statement](#). This statement should provide the following information, where applicable:

- Accession codes, unique identifiers, or web links for publicly available datasets
- A description of any restrictions on data availability
- For clinical datasets or third party data, please ensure that the statement adheres to our [policy](#)

All raw data has been uploaded to sequence read archive (accession pending). Processed duplex reads are deposited in zenodo.

## Human research participants

Policy information about [studies involving human research participants and Sex and Gender in Research](#).

### Reporting on sex and gender

*Use the terms sex (biological attribute) and gender (shaped by social and cultural circumstances) carefully in order to avoid confusing both terms. Indicate if findings apply to only one sex or gender; describe whether sex and gender were considered in study design whether sex and/or gender was determined based on self-reporting or assigned and methods used. Provide in the source data disaggregated sex and gender data where this information has been collected, and consent has been obtained for sharing of individual-level data; provide overall numbers in this Reporting Summary. Please state if this information has not been collected. Report sex- and gender-based analyses where performed, justify reasons for lack of sex- and gender-based analysis.*

### Population characteristics

*Describe the covariate-relevant population characteristics of the human research participants (e.g. age, genotypic information, past and current diagnosis and treatment categories). If you filled out the behavioural & social sciences study design questions and have nothing to add here, write "See above."*

### Recruitment

*Describe how participants were recruited. Outline any potential self-selection bias or other biases that may be present and how these are likely to impact results.*

### Ethics oversight

*Identify the organization(s) that approved the study protocol.*

Note that full information on the approval of the study protocol must also be provided in the manuscript.

## Field-specific reporting

Please select the one below that is the best fit for your research. If you are not sure, read the appropriate sections before making your selection.

- Life sciences     Behavioural & social sciences     Ecological, evolutionary & environmental sciences

For a reference copy of the document with all sections, see [nature.com/documents/nr-reporting-summary-flat.pdf](https://www.nature.com/documents/nr-reporting-summary-flat.pdf)

## Life sciences study design

All studies must disclose on these points even when the disclosure is negative.

Sample size	No sample size calculation was performed.
Data exclusions	No data were excluded from analyses.
Replication	Data were validated in other orthogonal datasets as well as multiple individuals.
Randomization	Randomization is not relevant to the study as there were no interventions performed.
Blinding	Blinding was not relevant to the study as there were no interventions performed.

## Reporting for specific materials, systems and methods

We require information from authors about some types of materials, experimental systems and methods used in many studies. Here, indicate whether each material, system or method listed is relevant to your study. If you are not sure if a list item applies to your research, read the appropriate section before selecting a response.

## Materials &amp; experimental systems

n/a	Involvement
<input checked="" type="checkbox"/>	<input type="checkbox"/> Antibodies
<input checked="" type="checkbox"/>	<input type="checkbox"/> Eukaryotic cell lines
<input checked="" type="checkbox"/>	<input type="checkbox"/> Palaeontology and archaeology
<input type="checkbox"/>	<input checked="" type="checkbox"/> Animals and other organisms
<input checked="" type="checkbox"/>	<input type="checkbox"/> Clinical data
<input checked="" type="checkbox"/>	<input type="checkbox"/> Dual use research of concern

## Methods

n/a	Involvement
<input checked="" type="checkbox"/>	<input type="checkbox"/> ChIP-seq
<input checked="" type="checkbox"/>	<input type="checkbox"/> Flow cytometry
<input checked="" type="checkbox"/>	<input type="checkbox"/> MRI-based neuroimaging

## Animals and other research organisms

Policy information about [studies involving animals](#); [ARRIVE guidelines](#) recommended for reporting animal research, and [Sex and Gender in Research](#)

Laboratory animals	Months old (mo.) C57BL/6J (M. Mus musculus): young brain (4-5 mo.); young heart (4 mo.); old brain, heart, and liver (18-19 mo.) AKR/J (M. Mus musculus): young brain, heart, and liver (4 mo.); old brain, heart, and liver (18 mo.) ALR/LtJ (M. Mus musculus): young brain, heart, and liver (4 mo.); old brain, heart, and liver (15-16 mo.) FVB/NJ (M. Mus musculus): young brain (2-3 mo.); young heart and liver (3-4 mo.); old brain, heart, and liver (19-22 mo.) NZB/B1NJ (M. mus. domesticus): young brain, heart, and liver (3 mo.); old brain, heart, and liver (21 mo.)
Wild animals	The study did not involve wild animals.
Reporting on sex	Sex was not considered in the study. All mice are female.
Field-collected samples	The study did not involve samples collected from the field.
Ethics oversight	Animal use and all methods were approved by the Animal Care and Use Committee (V242-7224. 122-5, Kiel, Germany). Experiments were performed in accordance with the relevant guidelines and regulations by certified personnel.

Note that full information on the approval of the study protocol must also be provided in the manuscript.